



Self-assembled nano-photosensitizer for targeted, activatable, and biosafe cancer phototheranostics



Ke Cheng ^{a,b}, Junyang Qi ^a, Jie Zhang ^b, Huangxu Li ^b, Xiaojie Ren ^b, Wenyu Wei ^b, Lingkuan Meng ^b, Jing Li ^b, Qianqian Li ^{a,d}, Huatang Zhang ^{c,***}, Wenbin Deng ^{a,***}, Hongyan Sun ^{b,e,**}, Lin Mei ^{a,d,*}

^a School of Pharmaceutical Sciences (Shenzhen), Shenzhen Campus of Sun Yat-sen University, Shenzhen, 518107, PR China

^b Department of Chemistry and COSDAF (Center of Super-Diamond and Advanced Films), City University of Hong Kong, 83 Tat Chee Avenue, Kowloon, Hong Kong SAR, PR China

^c School of Chemical Engineering and Light Industry, Guangdong University of Technology, Guangzhou, Guangdong, 510006, PR China

^d Tianjin Key Laboratory of Biomedical Materials/Key Laboratory of Biomaterials and Nanotechnology for Cancer Immunotherapy, Institute of Biomedical Engineering, Chinese Academy of Medical Sciences and Peking Union Medical College, Tianjin, 300192, PR China

^e Key Laboratory of Biochip Technology, Biotech and Health Centre, Shenzhen Research Institute of City University of Hong Kong, Shenzhen, 518057, PR China

ARTICLE INFO

Keywords:

Self-assembly
Nano-photosensitizer
Precise photodynamic therapy
Fluorescence/photoacoustic imaging
Cancer phototheranostics

ABSTRACT

Cancer treatment currently still faces crucial challenges in therapeutic effectiveness, precision, and complexity. Photodynamic therapy (PDT) as a non-invasive tactic has earned widespread popularity for its excellent therapeutic output, flexibility, and restrained toxicity. Nonetheless, drawbacks, including low efficiency, poor cancer specificity, and limited therapeutic depth, remain considerable during the cancer treatment. Although great effort has been made to improve the performance, the overall efficiency and biosafety are still ambiguous and unable to meet urgent clinical needs. Herein, this study integrates merits from previous PDT strategies and develops a cancer-targeting, activatable, biosafe photosensitizer. Owing to excellent self-assembly ability, this photosensitizer can be conveniently prepared as multifunctional nano-photosensitizers, namely **MBNPs**, and applied to *in vivo* cancer phototheranostics in “all-in-one” mode. This study successfully verifies the mechanism of **MBNPs**, then deploys them to cell-based and *in vivo* cancer PDT. Based on the unique cancer microenvironment, **MBNPs** achieve precise distribution, accumulation, and activation towards the tumor, releasing methylene blue as a potent photosensitizer for phototherapy. The PDT outcome demonstrates **MBNPs**’ superior cancer specificity, remarkable PDT efficacy, and negligible toxicity. Meanwhile, *in vivo* NIR fluorescence and photoacoustic imaging have been utilized to guide the PDT treatment synergistically. Additionally, the biosafety of the **MBNPs**-based PDT treatment is ensured, thus providing potential for future clinical studies.

1. Introduction

Photodynamic therapy (PDT) has been raised as a powerful technique for non-invasive cancer therapeutics [1,2]. Photosensitizers (PSs) serve as the vital element in this tactic, which can generate reactive oxygen species (ROS) such as singlet oxygen (${}^1\text{O}_2$) upon photo-irradiation, consequently ablating local pathological cells and tissues.

Several types of PSs have been reported over the decades, including organic fluorophores [3], transition metal coordination complexes [4], and semiconducting polymer nanoparticles (SPNs) [5,6]. Among these regular PSs, organic fluorophores are boosted as the most ubiquitous type, owing to their unique superiorities, including strong fluorescence properties, good biocompatibility and biodegradability, longer triplet lifetimes [7], and structural extension. So far, several organic

* Corresponding author. School of Pharmaceutical Sciences (Shenzhen), Shenzhen Campus of Sun Yat-sen University, Shenzhen, 518107, PR China.

** Corresponding author. Department of Chemistry and COSDAF (Center of Super-Diamond and Advanced Films), City University of Hong Kong, 83 Tat Chee Avenue, Kowloon, Hong Kong SAR, PR China.

*** Corresponding author.

**** Corresponding author.

E-mail addresses: htzhang@gdt.edu.cn (H. Zhang), dengwb5@mail.sysu.edu.cn (W. Deng), hongysun@cityu.edu.hk (H. Sun), meilin@bme.pumc.edu.cn (L. Mei).

fluorescent PSs, including porphyrin derivatives, chlorins, and phthalocyanine, have been applied to clinical studies [1]. Despite the widespread recognition, the organic fluorophore PSs still suffer from various issues, for example, poor water solubility, low cellular uptake, limited therapeutic depth, and weak cancer targeting. To improve their performance, small organic fluorescent PSs can be decorated with novel functionalities such as activatable [8–10], self-assemble [11–14], aggregate [15], fluorescence resonance energy transfer (FRET) [16], and cancer-targeting [17,18]. In general, the modern development of PSs tends to pursue more versatility, delicacy, and higher integration, which can be concluded as “all in one” or “one for all” strategies.

As a small phenothiazine-based near-infrared (NIR) fluorophore, methylene blue (MB) exhibits many advantages, such as small molecular size, superior water solubility, and high quantum yield in generating ROS. Therefore, it has been broadly used as a powerful PS for clinical cancer PDT [19]. Meanwhile, MB's biological safety is highly appreciated since it is an FDA-approved oxidation-reduction agent for treating methemoglobinemia, malaria, and vasoplegic syndrome [20]. Owing to its robust NIR fluorescence property, reliable biocompatibility, and biostability, MB is also widely applied in fluorescence imaging and staining [21,22]. Recently, methylene blue was demonstrated with highly efficient photoacoustic (PA) contrast property, enabling the construction of PA probes for sensing drug release and tumor microenvironment (e.g., ROS, biothiols) *in vivo* [23–25]. Compared with fluorescence imaging, photoacoustic (PA) imaging offers the advantage of deeper detection depth [26–29]. Despite these advantages, MB

demonstrates poor tumor targeting ability and cannot efficiently accumulate in the tumor site. These flaws may lead to low photosensitive potency and considerable toxicity towards normal cells and tissues, thus significantly impairing the therapeutic specificity and efficacy during the PDT treatment. Currently, several strategies have emerged to improve the PDT performance by chemical functionalization of MB. Typically, the most convenient way is to transform single MB into activatable probes. By this means, NIR irradiation [30], endogenous enzymes [31,32], and small intracellular molecules [23,33] may serve as the specific stimulus to trigger the probe and selectively release MB in the cancer region for precise PDT treatment. However, these strategies alone are insufficient for upgrading the overall therapeutic precision. Local accumulation of MB remains unsatisfied, thus resulting in limited PDT efficacy. Besides, the diffusion and metabolism of MB into the non-therapeutic cells and tissues still occur, bringing in potential risks during the cancer PDT treatment. In comparison, another feasible approach is to encapsulate MB with nanomaterials such as gold nanoparticles (AuNPs) [34], silver nanoparticles (AgNPs) [35], poly lactic-co-glycolic acid (PLGA) [36], silica nanoparticles (SiNPs) [37,38], and graphene [39]. With the help of these regular nanomaterials, MB can be encapsulated as nanoparticles with enhanced tumor targeting ability. Although these nanocarriers improve the enrichment of MB in the tumor, the encapsulation still has the risk of leakage, which may increase potential dark cytotoxicity. In addition, these nanocarriers are often inorganic or organic nanomaterials. Hence their biocompatibility and biodegradability require further consideration. Considering these

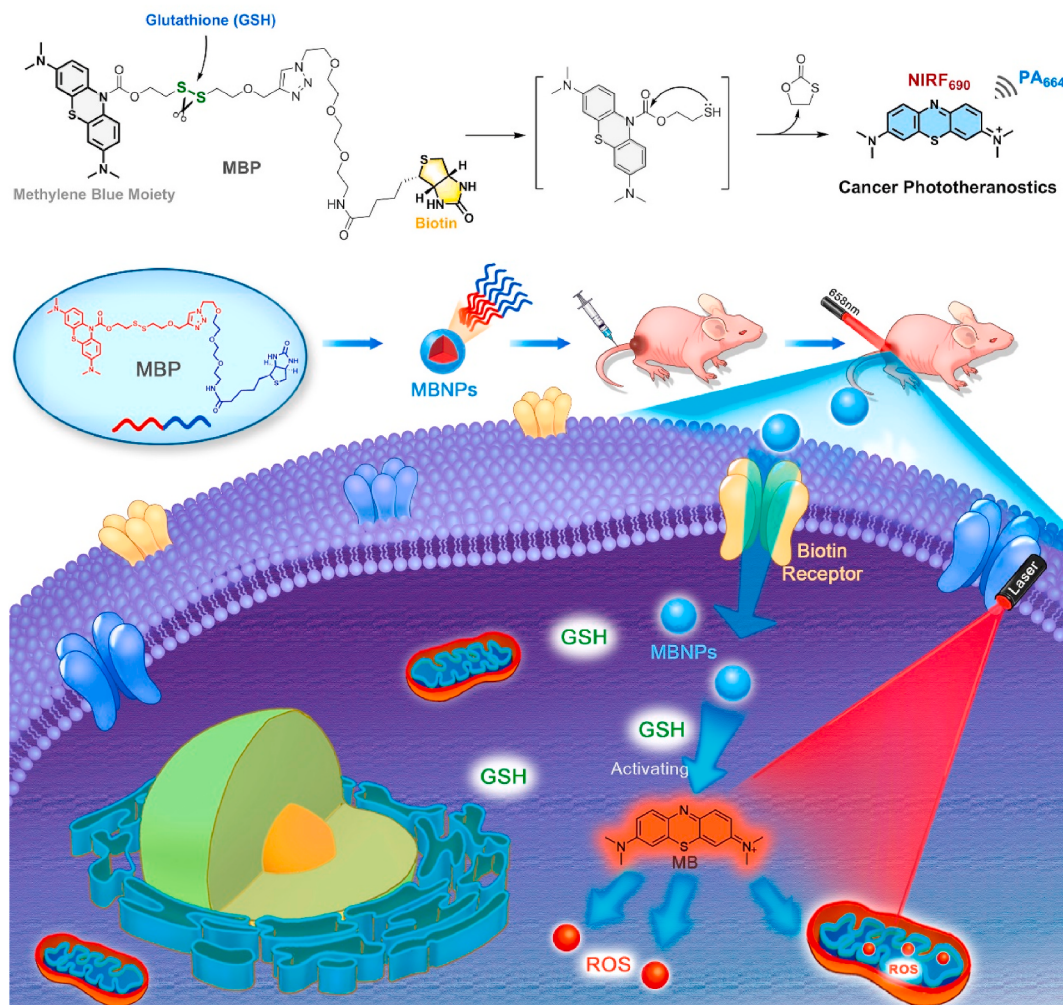


Fig. 1. Design, mechanism, and illustration of this work.

facts, a more sophisticated design is urgently desired to alter the single MB into a versatile PS, thus promoting its therapeutic specificity and efficacy and meeting the clinical needs.

Herein, for the first time, we report a rational molecular design by transforming MB into cancer-targeted, selectively activated, and self-assembled nano-photosensitizers, i.e., **MBNPs**. Theoretically, this design systematically integrates multiple cancer-targeting strategies with upgraded PDT tactics, based on the single MB molecular. As a result, a diagnostic and therapeutic nanoplatform containing cancer PDT treatment and NIR fluorescence/PA imaging has been proposed and shown in Fig. 1. Specifically, the MB moiety is structurally blocked by a disulfide trigger in its phenothiazine bridge via a carbamate bond. This modification transforms the MB into an uncharged, nonfluorescent, and hydrophobic form. The disulfide linker is responsive to the abundant glutathione (GSH) in cancer cells, which could release the reductive MB via an intramolecular elimination. The free reductive MB is active and can be oxidized promptly, offering the resulting oxidic, charged MB as potent PS in the local cancer environment. Given the high levels of GSH at the tumor site [40,41], this design could enable specific therapeutic action in the tumor microenvironment. Furthermore, the depletion of endogenous GSH levels by the disulfide bond can retain more ROS produced by the photosensitizers, thereby promoting the PDT efficacy [42–48]. To further improve the cancer-targeting ability and consider the overexpression of biotin receptors on the surface of cancer cells [49, 50], a hydrophilic biotin group could be conjugated to the other end of the disulfide linker, thus offering the resulting MB-based probe, namely **MBP**. Given the amphiphilicity of this molecular design, **MBP** could self-assemble in the aqueous phase system, forming homogeneous nanoparticles. Hence, the optimization of MB may endow the whole strategy with extra tumor-targeting ability, better biostability, and a higher cellular uptake ratio.

In summary, our design is expected with great cancer-targeting ability, relying on both the EPR (enhanced permeability and retention) effect and the biotin cancer-targeting group. Furthermore, the disulfide trigger can be selectively activated by excessive GSH in the cancer environment, thus releasing and accumulating free MB as powerful PS and fluorophore for precise phototherapy and responsive cancer imaging. Basically, by integrating complementary strategies and functionalities as many as possible into a single small NIR fluorophore-based PS, this work demonstrates an advanced “one for all” strategy for

novel, practical, biosafe, and highly efficient cancer phototheranostics.

2. Results and discussion

The proposed probe, **MBP**, was synthesized via three steps, including reduction of MB, coupling to a disulfide moiety, and click chemistry with biotin-azide (Fig. 2A). **MBP** and the intermediates (**S1**–**S3**) were successfully obtained and verified by HRMS and NMR (Supporting Information, Scheme S1–S4). With the **MBP** in hand, its amphiphatic property was first investigated. Interestingly, **MBP** exhibits poor solubility in aqueous solutions such as PBS and cell medium. Instead of directly precipitating out, **MBP** can be stably dispersed in these aqueous phases, resulting in a homogeneous and cloudy solution. Hence, we speculated that **MBP** might self-assemble in aqueous solutions and form stable homogenous nanoparticles, namely **MBNPs**. To verify this self-assembly phenomenon, TEM (transmission electron microscopy) imaging and DLS (dynamic light scattering) were used to characterize the morphology of the potential nanoparticles. **MBNPs** can be prepared by directly diluting the high concentration of **MBP** (10 mM) stocked in DMSO to 2–40 μM with deionized water, PBS, or cell medium, and self-assembly immediately occurs. As expected, homogeneous particles were observed in the TEM imaging (Fig. 2B), and the average lateral size was around 200 nm (Fig. 2C). Hence, the self-assembly ability of **MBP** was successfully proved, and **MBP** can be easily prepared as nanoformulation and applied to the following PDT tests.

Before the PDT tests, in vitro experiments were performed to evaluate the reaction between **MBNPs** and GSH. The reaction was first monitored by TEM imaging. **MBNPs** (5 μM) were first dispersed in PBS, and GSH (200 μM) was subsequently added. The mixture was incubated at 37 °C and continuously monitored for the morphological change with TEM imaging in different reaction stages. The results showed that as the reaction of **MBNPs** and GSH proceeded, the nanoparticles progressively collapsed, and the lateral size of the **MBNPs** continuously decreased (Fig. 2D). After 8 h incubation, all the nanostructures were destroyed, indicating a step-by-step activation and disassembling process from the surface of the nanoparticles by GSH.

Next, HPLC analysis was performed to measure the reaction rate of **MBNPs** with GSH. Briefly, **MBNPs** (200 μM) and GSH (2 mM) were mixed in PBS and incubated at 37 °C, and the mixture was monitored at different incubating periods by HPLC. The results showed that the **MBP**

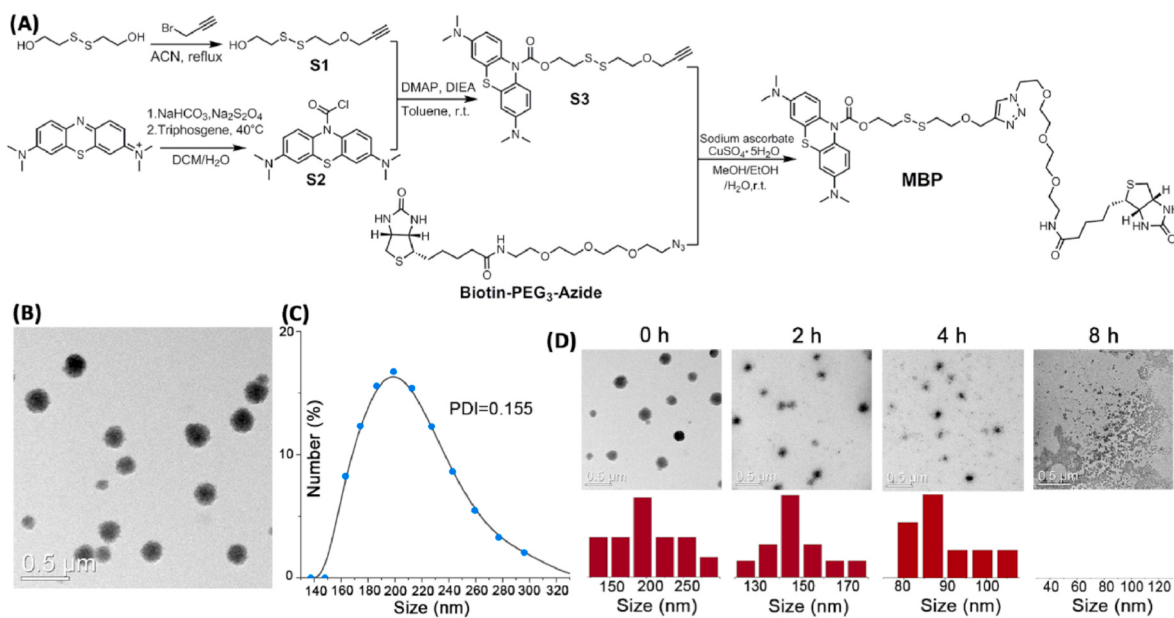


Fig. 2. (A) Synthetic scheme of **MBP**. (B) TEM image of **MBNPs**. (C) Size distribution of **MBNPs**, measured by DLS. (D) Analysis of **MBNPs**/GSH reaction by TEM imaging. Scale bar = 0.5 μm.

peak decreased as the incubation time increased until **MBP** was entirely consumed after 8 h (Fig. 3A). In the meantime, a new peak represented the **MB** product gradually raised in both 254 nm and 660 nm channels (Fig. S1A–B), suggesting the production of **MB** under the GSH condition. The absorbance and emission spectra of the reaction solutions were measured simultaneously. The spectra displayed time-dependently increased absorption ($\lambda_{\text{max}} = 664 \text{ nm}$) and emission ($\lambda_{\text{max}} = 690 \text{ nm}$) spectra as the reaction proceeded (Fig. S1C–D), demonstrating the time-dependent **MBNPs/GSH** reaction equilibrium. To better understand the reaction kinetics of **MBNPs** and GSH, in vitro dose-dependent and time-dependent analyses were further initiated. For the dose-dependent test, **MBNPs** (5 μM) were dissolved in 1 mL of PBS (pH = 7.4), and GSH was subsequently added in increasing concentration (0–200 μM). The mixtures were incubated at 37 °C for 2 h before the absorption and emission profiles were measured. As expected, the spectra exhibited noticeable boosts in both absorption ($\lambda_{\text{max}} = 664 \text{ nm}$) and emission ($\lambda_{\text{max}} = 690 \text{ nm}$) as the GSH concentration increased (Fig. 3B, Fig. S2A). Meanwhile, the relation between absorbance at 664 nm (A_{664}) or fluorescence at 690 nm (F_{690}) and the GSH concentration was characterized as linear (Fig. S2B–C). In addition, the fluorescent detection limit was calculated as 191 nM. For the time-dependent test, the results suggested that **MBNPs** (5 μM) reacted efficiently with GSH (200 μM) in 2 h, and the reaction rate was determined as 0.83 $\text{M}^{-1} \text{s}^{-1}$ (Fig. 3C, Fig. S3). After that, reaction selectivity tests were performed to assess the response of **MBNPs** to different potential interfering species. **MBNPs** (5 μM) were co-incubated with 100 μM of each analyte in PBS. The mixtures were further incubated at 37 °C for 2 h before the spectra were measured. Compared to other stimuli, superior reactivity towards biothiols, including Cys, Hcy, and GSH, was observed for **MBNPs** (Fig. 3D, Fig. S4).

Subsequently, in vitro tests were set to investigate the photosensitivity of **MBNPs** by evaluating ROS generation with 1,3-diphenylisobenzofuran (DPBF). As shown in Fig. 3E, the absorption of DPBF kept decreasing as the laser irradiation duration increased during the 20 min

test. Based on the absorbance change at 420 nm, the consumption of DPBF was determined as first-order kinetics (Fig. S5). Moreover, nearly 71.5% of the DPBF was consumed by the end of the test. Hence, these results implied the high ROS-generating ability of **MBNPs** under GSH and laser irradiation treatment. Additionally, in vitro PA tests were conducted to monitor the **MBNPs/GSH** reaction, considering the excellent PA property of **MB**. **MBNPs** were prepared in PBS in different concentrations (0–20 μM), and GSH (200 μM) was subsequently added. The mixtures were incubated at 37 °C for 8 h before the PA spectra were recorded. The PA results showed that under the GSH activation, the PA signals of **MB** could be detected, and the intensity increased linearly as the concentration of **MBNPs** increased (Fig. 3F), demonstrating the excellent PA responsive capability of **MBNPs**. The PA responsive ability of **MBNPs** (10 μM) was also measured with increasing amounts of GSH (Fig. S6). Likewise, the PA signal enhanced linearly as the concentration of GSH increased from 0 to 100 μM . Therefore, these PA results provided theoretical support for the further application of **MBNPs** in vivo cancer PA imaging.

Live-cell fluorescence imaging experiments were performed to investigate the cellular uptake, localization, and action of **MBNPs**. Time-dependent imaging was first conducted with HeLa cells, and the results suggested that **MBNPs** (2 μM) can be efficiently ingested by HeLa cells and progressively activated by endogenous GSH in 12 h (Fig. S8). The red **MB** fluorescence mainly distributed in the cytoplasm became observable within 2 h incubation and reached maximum intensity around 12 h. Hence, 12 h after the treatment of **MBNPs** was recognized as the optimal phase for cellular PDT experiments. Meanwhile, with the prior treatment of N-ethylmaleimide (NEM, 1 mM, a GSH scavenger) for 30 min, the fluorescence significantly dropped in HeLa and A549 cells (Fig. S9–10), suggesting the key role of GSH in the cellular action of **MBNPs**. After that, **MBNPs** were subsequently applied to a cellular imaging comparison between cancerous cells (HeLa, A549) and healthy, normal human cells (HDF, NP69). These cells were treated with **MBNPs** (2 μM) for 12 h, washed twice with PBS, and stained the nucleus before

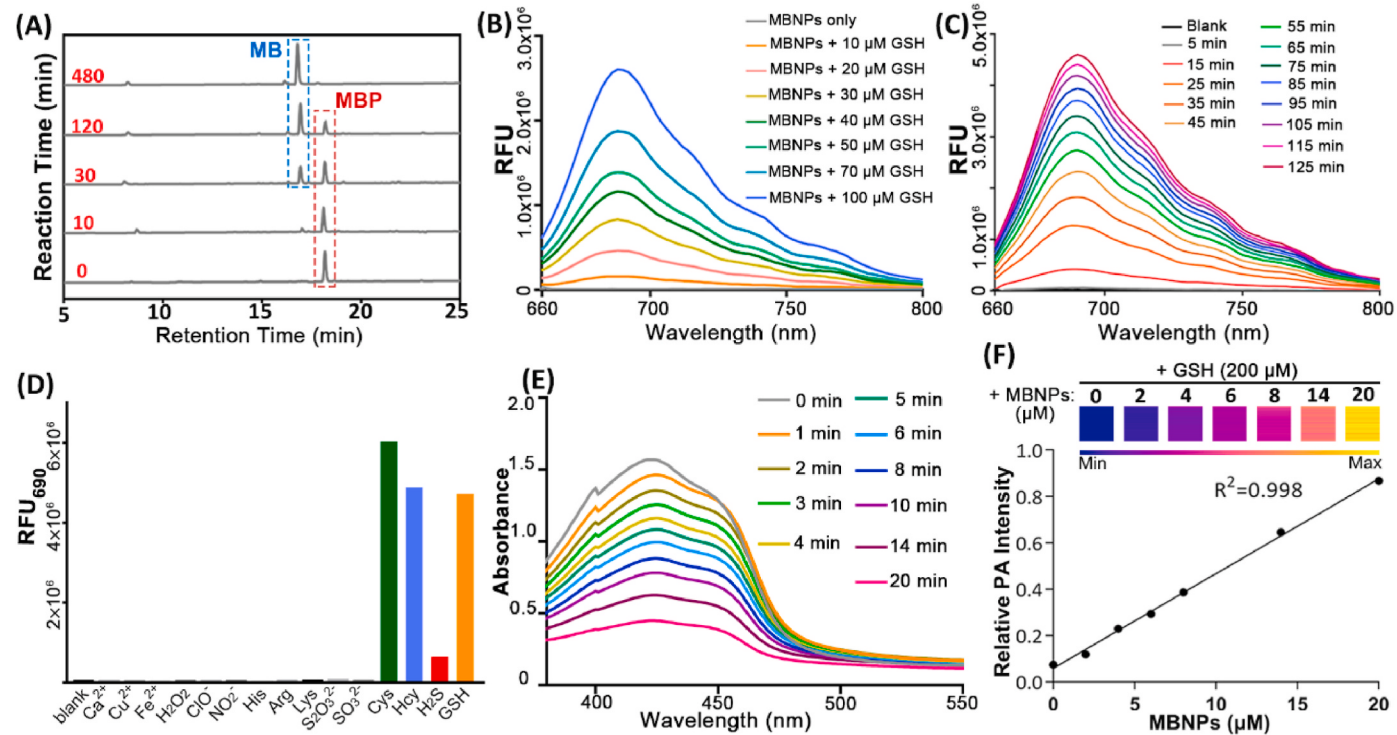


Fig. 3. (A) HPLC analysis of the **MBNPs/GSH** reaction (254 nm channel). (B) (C) Dose-dependent and time-dependent analysis of **MBNPs/GSH** reaction. (D) Reaction selectivity of **MBNPs** to different stimuli. (E) Evaluation of ROS generation of **MBNPs** (10 μM) with DPBF (20 $\mu\text{g/mL}$). (F) In vitro photoacoustic analysis of the **MBNPs** under 200 μM of GSH.

confocal imaging. Distinct fluorescence, representing the released MB, was observed in the cytoplasm of cancer cells (Fig. 4, Fig. S11), including HeLa and A549 cells. In sharp contrast, only faint MB fluorescence was seen in normal cells, i.e., HDF and NP69 cells. Hence, these imaging results demonstrated the remarkable specificity of **MBNPs** towards cancerous cells and neglectable interference on normal human cells. To better understand the different cellular actions of **MBNPs** in cancerous and normal cells, the intracellular GSH levels were determined by Ellman's reagent (DTNB) based on previous protocols [23,51]. As expected, significantly higher intracellular GSH levels were observed in cancerous cells than in normal cells, and the GSH levels can be reduced by treating **MBNPs** (Fig. S7). In addition, the cellular imaging of **MBNPs** was analyzed with HeLa cells in the presence of exogenous GSH and biotin (Fig. S12). It was observed that the responsive fluorescence was significantly enhanced by the addition of extrinsic GSH (1 mM), indicating the activation of **MBNPs** can be promoted by increasing intracellular GSH levels. Furthermore, excessive biotin (1 mM) was added as a competitor to interrupt the binding of **MBNPs** to the membrane biotin receptors during the cellular uptake process. As a result, the fluorescence was significantly inhibited, suggesting that **MBNPs** are highly likely to target cancer cells via the overexpressed biotin receptors. Overall, these cellular imaging results illustrate **MBNPs**' consistent self-assembly capability, robust GSH-reactivity, excellent cancer-targeting ability, and high photosensitizing potency, which bodes well for further PDT tests.

The in vitro tests and intracellular imaging have verified the GSH-triggering capability and high ROS generating efficiency of **MBNPs**, offering the potential for further application in cancer PDT. To this end, **MBNPs** were next applied to a series of cell-based PDT tests. The dark cytotoxicity and phototoxicity towards cancerous and normal cells were first measured with Cell Counting Kit-8 (CCK-8). To our surprise, MB

exhibited appreciable dark cytotoxicity towards HeLa and HDF cells (Fig. S13C). By contrast, **MBNPs** showed negligible dark cytotoxicity towards both normal cells (HDF, NP69) and cancerous cells (HeLa, A549) at high concentrations (Fig. S13A–B), indicating **MBNPs**' low cytotoxicity and excellent biosafety. This differentiable cytotoxicity is probably because of the specific properties of **MBNPs**, such as molecular neutrality, biocompatible nanoformulation, and smooth biological metabolism process. By contrast, MB is a fully charged and highly penetrable small molecule. Therefore, it may quickly spread into normal cells and cause acute toxicity at a high dose in local cellular substructures, such as mitochondria. As for phototoxicity, MB imposed high phototoxicity on both HDF and HeLa cells with no significant difference (Fig. S13C). In contrast, **MBNPs** exhibited no apparent phototoxicity towards HDF cells (Fig. 5A), which can be explained by the low specificity of **MBNPs** towards HDF cells as observed in the cellular imaging experiments. As the most ubiquitous cells in human dermis, HDF is particularly susceptible during the PDT treatment. Hence, the low dark and photo cytotoxicity of **MBNPs** on HDF cells could ensure the biosafety during the PDT treatment. Meanwhile, **MBNPs** displayed prominent phototoxicity and excellent PDT efficacy towards HeLa cells, which could be attributed to the superb cancer-targeting ability of **MBNPs** and more efficient cellular uptake by cancer cells over normal cells.

To further investigate the phototoxic mechanism, cellular ROS generation was next evaluated in detail. As expected, cells treated with **MBNPs** and laser irradiation presented significant cellular ROS levels (Fig. 5B and 5C) compared to no laser-treated cells. By treating exogenous GSH (1 mM), the resulting ROS levels decreased dramatically, which is likely due to the scavenging of ROS by additional GSH, although the high intracellular GSH levels may promote the activation of **MBNPs**. The cellular ROS levels were also evaluated in HDF cells. In

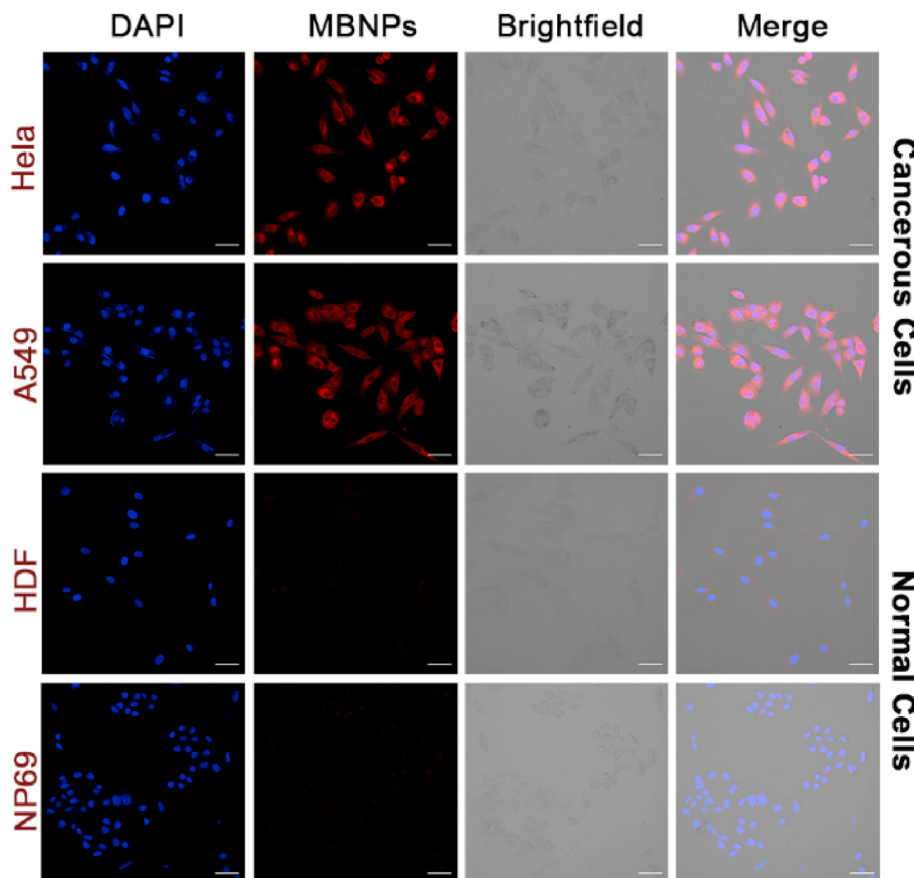


Fig. 4. Cellular imaging of **MBNPs** (2 μ M) in cancerous and normal cells. Scale bar = 50 μ m.

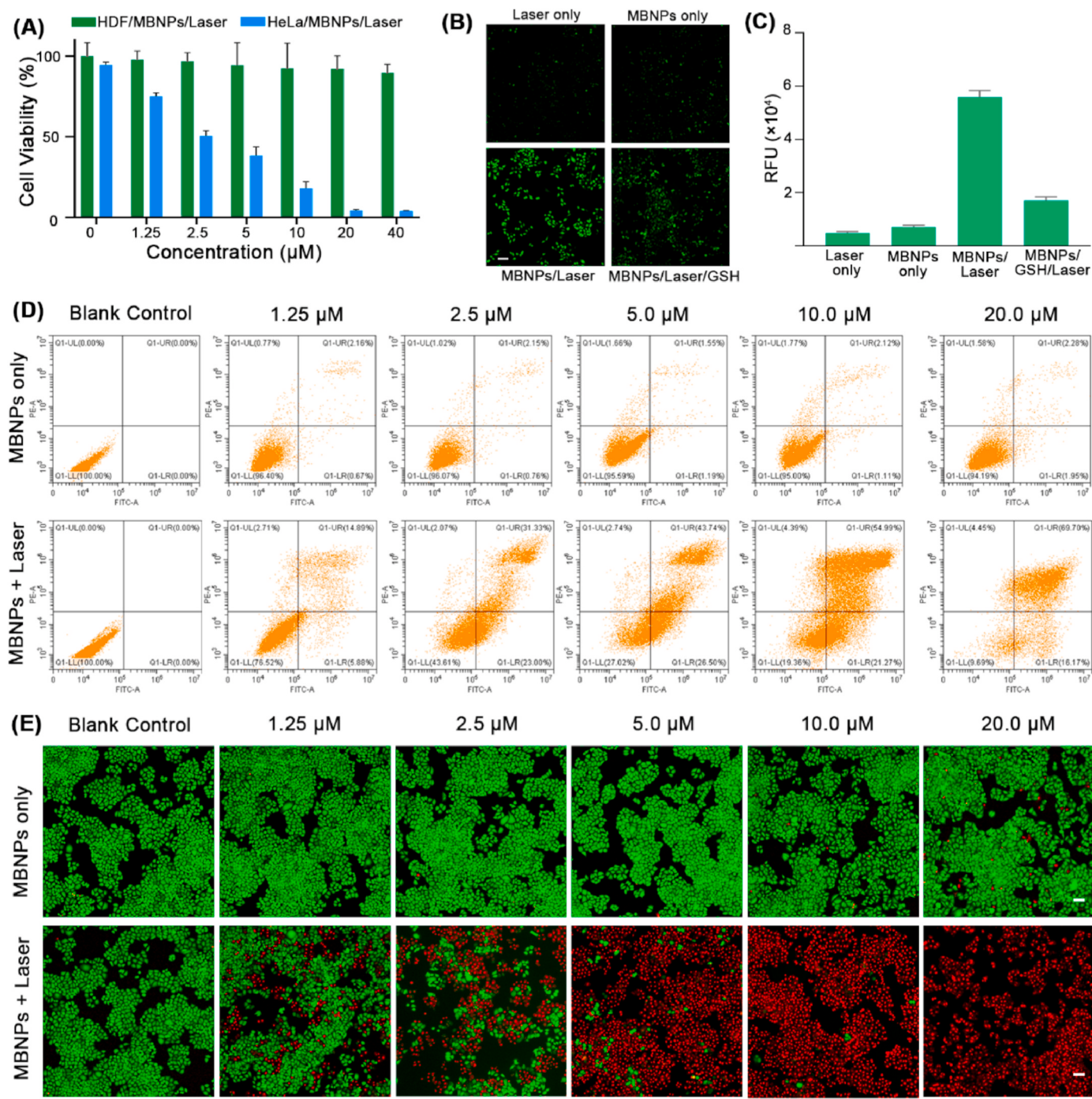


Fig. 5. (A) Cell viability of HeLa and HDF cells treated with NIR laser irradiation (658 nm, 0.5 W/cm²) and MBNPs at different concentrations. Data represent mean \pm SEM ($n = 5$). (B) Cellular ROS evaluation of MBNPs (20 μM) by H₂DCFDA (10 μM) in HeLa cells. Scale bar = 100 μm . (C) Fluorescence quantification in (B). (D) Flow cytometry analysis of cell-based PDT with MBNPs. (E) Calcein-AM (green) and propidium iodide (PI, red) analysis of the cells underwent the MBNPs-based PDT tests. Scale bar = 100 μm . (For interpretation of the references to colour in this figure legend, the reader is referred to the Web version of this article.)

sharp contrast, the treatment of MBNPs and laser did not significantly increase the ROS levels in HDF cells (Fig. S14). These results may explain the high phototoxicity of MBNPs on cancer cells and low phototoxicity on normal cells, as observed in the cell viability tests. Next, flow cytometry analysis verified the apoptosis of cancer cells induced by the co-treatment of MBNPs and laser irradiation. As shown in Fig. 5D, no apparent cell apoptosis was seen in blank control or dark-treated groups. However, the apoptosis became appreciable under co-treatment of MBNPs and laser irradiation, and the apoptotic levels increased with the treatment of more MBNPs. Ultimately, most cancer

cells were killed by treating 20 μM of MBNPs and 10 min of laser treatment. Likewise, the live and dead dual-stain was performed with a fluorometric Calcein-AM and PI assay to estimate the cell-based PDT efficacy of MBNPs. As a result, the staining proved the excellent cellular PDT efficacy of MBNPs (Fig. 5E). For laser-treated groups, the cell apoptosis turned appreciable with 1.25 μM of MBNPs and reached saturated by treating 20 μM of MBNPs. By that time, nearly all cancer cells were killed. By contrast, all MBNPs-only treated groups (no laser) displayed negligible cell apoptosis or cytotoxicity. Hence, these cell-based PDT results demonstrate the high cancer-targeting ability,

superior PDT efficacy, and excellent biosafety of **MBNPs**, providing prospects for the following *in vivo* PDT studies.

Encouraged by the cell-based PDT outcomes of **MBNPs**, *in vivo* time-resolved fluorescence imaging was then performed to evaluate the distribution and accumulation of **MBNPs** in tumor-bearing nude mice, which may reveal the accurate tumor location and specify the biological metabolism of **MBNPs**, thus guiding the *in vivo* PDT tests. The model mice (female BALB/c nude mice with HeLa tumor) were prepared and injected intravenously with the freshly prepared **MBNPs** (20 μ M in 100 μ L PBS). After the injection, the mice were monitored with the animal imaging system. The *in vivo* fluorescence imaging was acquired and shown in Fig. 6A. The fluorescence appeared first in the kidney area, then gradually accumulated in the tumor area after injection, and reached the highest level after 12 h. Later, the fluorescence signal decreased as the MB was eliminated via the kidney and liver after 24 h. Meanwhile, the major organs and tumors of mice treated with **MBNPs** for 12 h were resected for *ex vivo* fluorescence imaging. As expected, the *ex vivo* fluorescence imaging results exhibited the most vigorous fluorescence intensity in the tumor region, while lower fluorescence was seen in other organs (Fig. 6B–C). For a comprehensive assessment of the internal metabolism of **MBNPs**, *in vivo* PA imaging was next utilized to image the deeper region of the tumor. The PA imaging at the tumor site was captured and analyzed after tail vein injection of **MBNPs** (20 μ M in 100 μ L PBS). Similarly, the activation and accumulation of MB in the tumor area were observable 2 h after the injection of **MBNPs**, and the PA intensity was time-dependent and reached the maximum level within 12 h (Fig. 6D). The released MB were then gradually metabolized and eventually eliminated in 36 h. According to the PA signal intensity quantification (Fig. 6E), the strongest PA signal was noticed around 12 h after the injection, implying the optimal phototherapeutic stage. Altogether, *in vivo* fluorescence and PA imaging successfully demonstrate

MBNPs' excellent cancer-targeting capability, cancer responsive reactivity, and favorable biodegradability, which offers a powerful approach for tumor imaging and instructs the succeeding *in vivo* PDT experiments.

Inspired by these *in vivo* fluorescence and PA imaging results, **MBNPs** were finally applied to *in vivo* cancer PDT experiments. The female BALB/c nude mice bearing HeLa tumor were established as the cancer model and treated intravenously with freshly prepared **MBNPs** (20 μ M in 100 μ L PBS). After 12 h, the tumor area was irradiated with the 658 nm laser for 10 min. Mice's body weight and the tumor volume were recorded every two days until sacrificed on day 14. The tumor from each group was extracted and photographed respectively. According to the relative tumor volume change shown in Fig. 7A, the tumor growth was significantly suppressed by the treatment of **MBNPs** and laser irradiation. Consequently, mice treated with **MBNPs** and laser exhibited far less tumor weight and volume than other control groups on day 14 (Fig. 7B–C). In contrast, control mice, including the dark-treated or laser-only-treated, gained significant tumor growth during the 14 days. Of note, no apparent body weight loss was seen for all mice (Fig. 7D), indicating the negligible toxicity of these therapeutic regimens on the mice. Next, H&E (Hematoxylin and eosin) stain and TUNEL (Terminal deoxynucleotidyl transferase dUTP nick end labeling) assay were conducted to inspect the necrosis and apoptosis levels inside tumor tissues induced by the PDT treatments. As shown in Fig. 7E, cells of cancer tissues that underwent the **MBNPs**-based PDT treatment were transformed from original fiddle-shaped or polygonal smaller to round, nuclear pyknosis or fragmentation. By comparison, no significant transformation was noticed for other control groups. For TUNEL analysis, compared with mice from control groups, high tumor necrosis levels and massive TUNEL-positive cells were noted in **MBNPs** and laser co-treated mice. These results suggested the high efficiency of **MBNPs** in

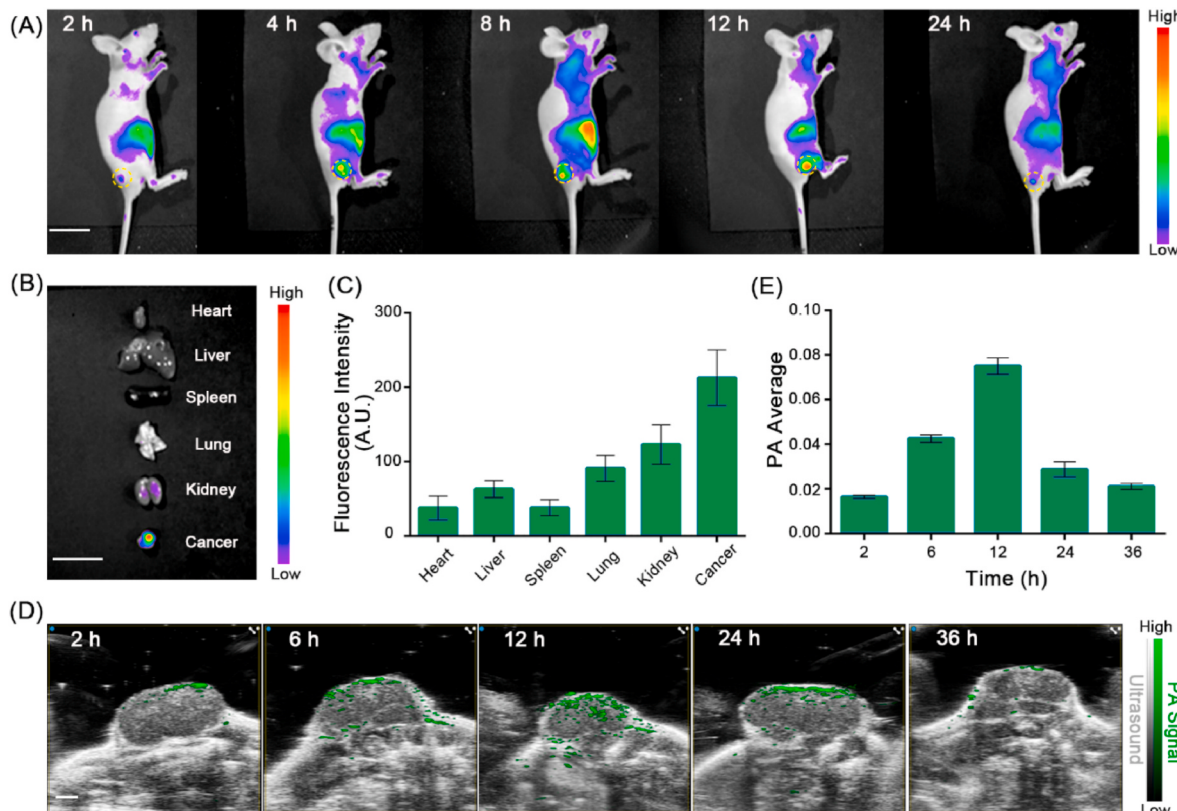


Fig. 6. (A) Time-resolved *in vivo* fluorescence imaging of **MBNPs** on tumor-bearing mice. Scale bar = 20 mm. Tumors were indicated in yellow circles. (B) Fluorescence imaging of individual tumors and organs after systemic administration with **MBNPs** for 12 h. Scale bar = 20 mm. (C) Fluorescence quantification in (B). (D) *In vivo* PA imaging of **MBNPs**. Scale bar = 2 mm. (E) Quantification of the PA signals in (D). (For interpretation of the references to colour in this figure legend, the reader is referred to the Web version of this article.)

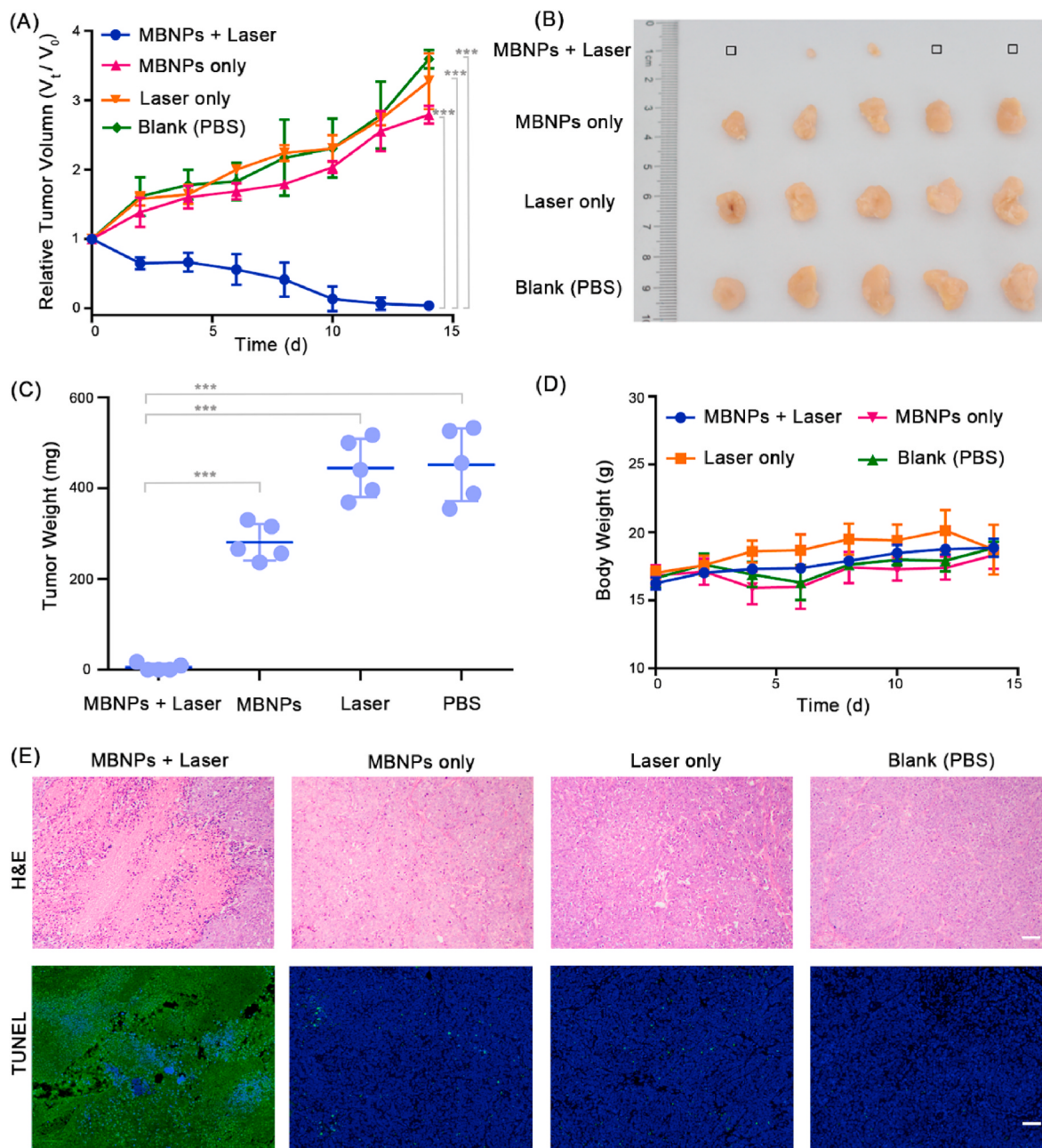


Fig. 7. (A) Relative tumor volume change in 14 days after the treatment with different formulations ($n = 5$; mean \pm SEM; *** $p < 0.001$). (B) Tumor images on day 14 after the PDT treatment. (C) Tumor weight on day 14 after the PDT tests. (D) Body weight change of each group in 14 days. (E) Tumor slices with H&E staining and TUNEL analysis of the tumor tissues after the PDT tests. Scale bar = 100 μ m.

inducing cancer cell necrosis and apoptosis during the PDT experiments. In addition, tissues of major organs, including the heart, liver, spleen, lung, and kidney, were collected from mice that underwent the PDT experiments for H&E stain to assess possible histological changes. The results showed no evident damage to tissues or organs in all groups after the corresponding treatments (Fig. S15), suggesting insignificant histological abnormalities or lesions. At last, the routine blood tests were systematically established to examine the side effects and overall interference of the in vivo PDT treatment. All parameters remained at normal levels for the mice, implying that no apparent infection or inflammation was caused by the PDT treatments (Fig. S16). Overall, these results demonstrate the excellent therapeutic efficacy of **MBNPs** for in vivo cancer PDT and prove the reliable biological safety and biocompatibility of this versatile nano-photosensitizer.

3. Conclusion

To summarize, we have developed a GSH-triggered, activatable, and cancer-targeting probe, **MBP**, based on our rational design of a small NIRF photosensitizer, methylene blue. This multifunctional probe can self-assemble and present as nano-photosensitizer, **MBNPs**. Hence, an “all-in-one” cancer phototheranostic strategy with multiple cancer-targeting abilities and upgraded PDT mode has been proposed and established. The specific activation of **MBNPs** by GSH has been successfully verified by a series of in vitro tests. Then, **MBNPs** were applied to cellular experiments to investigate their action and mechanism in cancer cells. As expected, cellular imaging of **MBNPs** displays excellent specificity and high functionality towards cancer cells. Meanwhile, cellular PDT results demonstrate the high therapeutic precision and superior PDT efficacy of **MBNPs**. Hence, this nano-photosensitizer was

finally applied to in vivo imaging-guided cancer PDT experiments. In vivo fluorescence and PA imaging illustrate the distribution and biological action of **MBNPs** in tumor-bearing mice. Based on the imaging guidance, **MBNPs** can be smoothly implemented in mice model-based PDT tests. Consequently, in vivo PDT experiments demonstrate the remarkable PDT efficacy and precision of **MBNPs** in tumor ablation. Meanwhile, the biological safety of the PDT treatment with **MBNPs** has been assured. Overall, this study has developed a versatile small fluorophore-based nano-photosensitizer integrated with multiple cancer therapeutic properties. This “all-in-one” tactic achieves synergistic fluorescence/PA-guided cancer phototheranostics with superior qualities, including good biosafety, excellent therapeutic efficacy, and high therapeutic precision. It is anticipated that this nano-photosensitizer and strategy could eventually be applied to future clinical studies for cancer treatment.

4. Methods

4.1. Materials and instruments

Vendor information for chemicals used in this study: methylene blue (methylthioninium chloride, Sigma-Aldrich); 2,2'-disulfanediylbis(ethan-1-ol) (Sigma-Aldrich); 3-bromoprop-1-yne (J&K); sodium dithionite (Sigma-Aldrich); N,N-diisopropylethylamine (DIEA, J&K); glutathione (GSH, Sigma-Aldrich); copper sulfate pentahydrate (Sigma-Aldrich); Sodium bicarbonate (Sigma-Aldrich); bis(trichloromethyl) carbonate (triphosgene, J&K); 4-dimethylaminopyridine (DMAP, J&K); Biotin-PEG₃-Azide (Sigma-Aldrich); 5,5-dithio-bis-(2-nitrobenzoic acid (DTNB, Sigma-Aldrich); sodium ascorbate (Sigma-Aldrich); N-ethyl-maleimide (NEM, J&K); D-biotin (Acros); 1,3-diphenylisobenzofuran (DPBF, Sigma-Aldrich). 2',7'-dichlorodihydrofluorescein diacetate (H₂DCFDA, Sigma-Aldrich). All chemical reagents were obtained from vendors and used without purification. CCK-8 and Calcein-AM/PI Assay were purchased from Dojindo. Dead Cell Apoptosis Kit was supplied by KeyGen Biotech. H&E Stain and TUNEL Kit were obtained from Abcam. 658 nm NIR laser was supplied by Xi'an Bohr Optoelectronics Technology. The laser power was used at 0.5 W/cm² in this study. TEM imaging was conducted on JEM-2010HR (200 kV).

4.2. ROS determination

MBNPs (10 μM) and GSH (200 μM) were mixed and incubated in PBS at 37 °C for 2 h. Then, the mixture was irradiated with the 658 nm laser for 20 min after 1,3-diphenylisobenzofuran (DPBF, 20 μg/mL) was added, and the absorption spectra were measured continuously.

4.3. Cellular imaging

Cells were seeded in the dishes with glass bottoms and grown to 50% confluence. Next, cells were treated with freshly prepared **MBNPs** (2 μM) in the cell medium in the presence or absence of inhibitors (NEM, biotin). After incubation for 12 h, the cells were gently washed three times with PBS, followed by nucleus staining. Fluorescence images were then captured on confocal microscopy (LSN880, Zeiss).

4.4. Estimation of intracellular GSH levels

Cells were seeded in the dishes and grown to 80% confluence. Cells were then treated with fresh medium with/without **MBNPs** (20 μM) for 12 h. Next, cells were washed with PBS, digested with trypsin, and collected for cell number calculation. Cells (5 × 10⁶) were lysed with 200 μL of RIPA lysis buffer on ice for 30 min. After centrifugation at 4 °C for 15 min (10,000 rpm), the supernatant was collected. 10 μL of the resulting lysate was mixed with 50 μL of DTNB (0.5 mM in PBS) and incubated at r.t. for 15 min before the absorbance at 405 nm was measured by a plate reader. The GSH concentration of the lysate was

calculated based on a standard GSH/DTNB absorbance curve measured under identical conditions.

4.5. Cell viability assay

For the dark toxicity, cells were transferred to 96-well microplates (5000 cells per well) to adhere overnight, followed by incubation under MB or **MBNPs** (0–40 μM) containing medium for 24 h. Then, the CCK-8 reagent (10 μL/well) was added and incubated for 30 min. Afterward, the plates were applied to a plate reader (VICTOR NivoTM Multimode Plate Reader, PerkinElmer) to detect the absorbance at 450 nm (A₄₅₀). For phototoxicity, the cells were treated with MB or **MBNPs** containing medium for 12 h before being irradiated with the laser for 10 min, followed by further 12 h culture, treatment of CCK-8, and absorbance determination. Cell viability was calculated as V = (A - A₀)/(A_s - A₀) × 100%. A represents the A₄₅₀ of MB/**MBNPs** treated groups, A_s represents the A₄₅₀ of the DMSO group, and A₀ represents the A₄₅₀ of the blank group.

4.6. Intracellular ROS evaluation

The cellular ROS levels were determined by Cellular ROS Assay Kit. HeLa or HDF cells were cultured in 12-well plates (5 × 10⁴ cells per well) for confluence. The next day, cells were washed with PBS and then treated with freshly prepared **MBNPs**-containing medium (20 μM) for 12 h. Subsequently, the cells were treated with 2',7'-dichlorodihydro-fluorescein diacetate (10 μM, H₂DCFDA) in the dark for 20 min. Then, the cells were rewash with PBS, and the experimental group was irradiated with the 658 nm laser for 10 min. Finally, the cells were deployed to a fluorescence microscope for imaging and quantified by ImageJ.

4.7. Cell apoptosis analysis

The cell apoptosis was investigated with Dead Cell Apoptosis Kit. HeLa cells were grown in 12-well microplates (5 × 10⁴ cells/well) to adhere, followed by treatment of **MBNPs**-containing medium (0–20 μM) for 12 h. Subsequently, experimental groups were treated with the laser for 10 min. After that, Cells were cultured for another 24 h before analysis by flow cytometry (CytoFLEX).

4.8. Calcein-AM/PI assay

The cell-based PDT efficiency of **MBNPs** was estimated by the Calcein-AM/PI Assay. HeLa cells were first grown in 12-well microplates (10⁵ cells/well). Following that, the cells were treated with **MBNPs** containing medium (0–20 μM) for 12 h. Laser irradiation (10 min) for experimental groups was conducted. The cells were further cultured for 24 h before Calcein-AM/PI stain and visualization by fluorescence microscope (Eclipse Ti2, NIKON).

4.9. Establishment of tumor mouse model

In vivo experiments were authorized by the Administrative Committee on Animal Research, Sun Yat-sen University (Approval No. SYSU-IACUC-2020-000321). Female BALB/c Nude mice (4–5 weeks) were obtained and fed in the pathogen-free animal room. HeLa cells (100 μL, 10⁶ cells) were subcutaneously injected into the right hip of the mice to initialize the xenograft model. The tumor volume (V_t) was measured as: V_t = 0.5 × length × width². V_t/V₀ was the relative tumor volume. V₀ is the original tumor volume before the phototherapy. The PDT experiments were launched as the volume reached 100 mm³.

4.10. In vivo fluorescence and PA imaging

The female BALB/c Nude mice were treated intravenously with

freshly prepared **MBNPs** (20 μM in 100 μL PBS). The tumor and main organs were inspected at different duration by an *in vivo* imaging system (Night OWL II LB 983, Bertold). For PA imaging, the mice were treated with **MBNPs** (20 μM in 100 μL PBS) via intravenous injection and monitored by a small animal PA imaging system (Vevo LAZR Imaging System, Fujifilm VisualSonics) at different stages.

4.11. In vivo PDT experiments

The mice were divided into 4 groups randomly ($n = 5$) before treating with the following schemes via intravenous injection respectively: (1) **MBNPs** (20 μM in 100 μL PBS) with laser irradiation; (2) **MBNPs** (20 μM in 100 μL PBS) without laser irradiation; (3) Laser irradiation only; (4) PBS only (100 μL). 12 h after the injection, mice from schemes (1) and (3) were irradiated with the laser (658 nm) for 10 min. Tumor volumes and body weights were recorded every 2 days until the mice were sacrificed on day 14, and the tumor was isolated and imaged.

4.12. Histopathological and immunohistochemical analysis

After the PDT experiments, the H&E stain and TUNEL analysis were performed to evaluate the apoptosis and necrosis levels in tumor tissues. The mice were sacrificed on day 14, and the major organs were collected and sliced for H&E and TUNEL staining. Then, stained slices were examined and imaged with microscopy.

4.13. Blood routine examination

Blood samples of mice from the PDT experiments were collected from the eye sockets on day 14. The standard hematology markers were measured, including white blood cells, lymphocytes, monocytes, neutrophilic granulocytes, lymphocyte percentage, monocyte percentage, neutrophilic granulocyte percentage, red blood cells, hematocrit, mean corpuscular volume, RBC distribution width-CV, and platelet count.

Credit author statement

Ke Cheng: Conceptualization, Methodology, Investigation, Data Curation, Formal Analysis, Writing-Review & Editing. Junyang Qi: Methodology, Investigation, Data Curation, Formal Analysis, Writing-Review & Editing. Jie Zhang: Conceptualization, Methodology, Investigation, Formal Analysis, Writing-Review & Editing. Huangxu Li, Xiaojie Ren: Investigation, Resources. Wenyu Wei, Jing Li, and Qianqian Li: Resources, Validation. Lingkuan Meng: Software. Huatang Zhang: Project Administration, Writing-Review & Editing. Wenbin Deng: Resources, Writing-Review & Editing. Hongyan Sun: Supervision, Resources, Project Administration, Writing-Review & Editing. Lin Mei: Supervision, Resources, Project Administration, Writing-Review & Editing.

Declaration of competing interest

The authors declare that they have no known competing financial interests or personal relationships that could have appeared to influence the work reported in this paper.

Data availability

Data will be made available on request.

Acknowledgments

K.C., J.Q., and J.Z. contributed equally to this work. The authors thank the financial support from the National Natural Science

Foundation of China (Grant Nos. 22078067, 21807014, 81971081, 31922042 and 82272154), National Natural Science Excellent Young Scientists Fund of China (Hong Kong and Macau) (Grant No. 32122003), Research Grants Council of Hong Kong (Grant Nos. 11102719 and 11302320), the Science Technology and Innovation Committee of Shenzhen Municipality (Grant No. JCYJ20180507181654823, GXWD20201231165807008.20200825175848001), the Guangdong Basic and Applied Basic Research Foundation (2020A1515011463 and 2020A1515010986), and the Pearl River Talent Plan of Guangdong Province (2017GC010596).

Appendix A. Supplementary data

Supplementary data to this article can be found online at <https://doi.org/10.1016/j.biomaterials.2022.121916>.

References

- [1] P. Agostinis, K. Berg, K.A. Cengel, T.H. Foster, A.W. Girotti, S.O. Gollnick, S. M. Hahn, M.R. Hamblin, A. Juuzeniene, D. Kessel, M. Korbeklik, J. Moan, P. Mroz, D. Nowis, J. Piette, B.C. Wilson, J. Golab, Photodynamic therapy of cancer: an update, *Ca-Cancer, J. Clin.* 61 (2011) 250–281.
- [2] D.E.J.G.J. Dolmans, D. Fukumura, R.K. Jain, Photodynamic therapy for cancer, *Nat. Rev. Cancer* 3 (2003) 380–387.
- [3] X. Zhao, J. Liu, J. Fan, H. Chao, X. Peng, Recent progress in photosensitizers for overcoming the challenges of photodynamic therapy: from molecular design to application, *Chem. Soc. Rev.* 50 (2021) 4185–4219.
- [4] S. Monro, K.L. Colon, H. Yin, J. Roque 3rd, P. Konda, S. Gujar, R.P. Thummel, L. Lilge, C.G. Cameron, S.A. McFarland, Transition metal complexes and photodynamic therapy from a tumor-centered approach: challenges, opportunities, and highlights from the development of TLD1433, *Chem. Rev.* 119 (2019) 797–828.
- [5] Y. Jiang, J. Li, Z. Zeng, C. Xie, Y. Lyu, K. Pu, Organic photodynamic nanoinhibitor for synergistic cancer therapy, *Angew. Chem. Int. Ed.* 58 (2019) 8161–8165.
- [6] J. Li, J. Rao, K. Pu, Recent progress on semiconducting polymer nanoparticles for molecular imaging and cancer phototherapy, *Biomaterials* 155 (2018) 217–235.
- [7] J. Zhao, W. Wu, J. Sun, S. Guo, Triplet photosensitizers: from molecular design to applications, *Chem. Soc. Rev.* 42 (2013) 5323–5351.
- [8] X. Li, S. Kolemen, J. Yoon, E.U. Akkaya, Activatable photosensitizers: agents for selective photodynamic therapy, *Adv. Funct. Mater.* 27 (2017), 1604053.
- [9] T.C. Pham, V.N. Nguyen, Y. Choi, S. Lee, J. Yoon, Recent strategies to develop innovative photosensitizers for enhanced photodynamic therapy, *Chem. Rev.* 121 (2021) 13454–13619.
- [10] C. Yao, Y. Li, Z. Wang, C. Song, X. Hu, S. Liu, Cytosolic NQO1 enzyme-activated near-infrared fluorescence imaging and photodynamic therapy with polymeric vesicles, *ACS Nano* 14 (2) (2020) 1919–1935.
- [11] W. Asahi, R. Kurihara, K. Takeyama, Y. Umebara, Y. Kimura, T. Kondo, K. Tanabe, Aggregate formation of BODIPY-tethered oligonucleotides that led to efficient intracellular penetration and gene regulation, *ACS Appl. Bio Mater.* 2 (2019) 4456–4463.
- [12] D. Chen, Q. Tang, J. Zou, X. Yang, W. Huang, Q. Zhang, J. Shao, X. Dong, pH-responsive PEG-doxorubicin-encapsulated Aza-BODIPY nanotherapeutic agent for imaging-guided synergistic cancer therapy, *Adv. Healthcare Mater.* 7 (2018), 1701272.
- [13] Y. Zhang, Z. Yang, X. Zheng, L. Chen, Z. Xie, Highly efficient near-infrared BODIPY phototherapeutic nanoparticles for cancer treatment, *J. Mater. Chem. B* 8 (2020) 5305–5311.
- [14] X. Hu, J. Hu, J. Tian, Z. Ge, G. Zhang, K. Luo, S. Liu, Polyprodrug amphiphiles: hierarchical assemblies for shape-regulated cellular internalization, trafficking, and drug delivery, *J. Am. Chem. Soc.* 135 (46) (2013) 17617–17629.
- [15] Z. Zhuang, J. Dai, M. Yu, J. Li, P. Shen, R. Hu, X. Lou, Z. Zhao, B.Z. Tang, Type I photosensitizers based on phosphindole oxide for photodynamic therapy: apoptosis and autophagy induced by endoplasmic reticulum stress, *Chem. Sci.* 11 (2020) 3405–3417.
- [16] L. Huang, Z. Li, Y. Zhao, J. Yang, Y. Yang, A.I. Pendharkar, Y. Zhang, S. Kelmar, L. Chen, W. Wu, J. Zhao, G. Han, Enhancing photodynamic therapy through resonance energy transfer constructed near-Infrared photosensitized nanoparticles, *Adv. Mater.* 29 (2017), 1604789.
- [17] B. Li, H. Xiao, M. Cai, X. Li, X. Xu, S. Wang, S. Huang, Y. Wang, D. Cheng, P. Pang, H. Shan, X. Shuai, Molecular probe crossing blood-brain barrier for bimodal imaging-guided photothermal/photodynamic therapies of intracranial glioblastoma, *Adv. Funct. Mater.* 30 (2020), 1909117.
- [18] D. Li, X.Z. Wang, L.F. Yang, S.C. Li, Q.Y. Hu, X. Li, B.Y. Zheng, M.R. Ke, J.D. Huang, Size-tunable targeting-triggered nanophotosensitizers based on self-assembly of a phthalocyanine-biotin conjugate for photodynamic therapy, *ACS Appl. Mater. Interfaces* 11 (2019) 36435–36443.
- [19] J.P. Tardivo, F. Adami, J.A. Correa, M.A. Pinhal, M.S. Baptista, A clinical trial testing the efficacy of PDT in preventing amputation in diabetic patients, *Photodiagnosis Photodyn. Ther.* 11 (2014) 342–350.
- [20] P.R. Ginimuge, S.D. Jyothi, Methylene blue: revisited, *J. Anaesthesiol. Clin. Pharmacol.* 26 (2010) 517–520.

- [21] C. Zhang, D. Jiang, B. Huang, C. Wang, L. Zhao, X. Xie, Z. Zhang, K. Wang, J. Tian, Y. Luo, Methylene blue-based near-infrared fluorescence imaging for breast cancer visualization in resected human tissues, *Technol. Cancer Res. Treat.* 18 (2019), 1533033819894331.
- [22] C. Zhang, Y. Mao, K. Wang, J. Tian, The identification of breast cancer by near-infrared fluorescence imaging with methylene blue, *J. Clin. Oncol.* 36 (2018) 12591, 12591.
- [23] Q. Zeng, R. Zhang, T. Zhang, D. Xing, H₂O₂-responsive biodegradable nanomedicine for cancer-selective dual-modal imaging guided precise photodynamic therapy, *Biomaterials* 207 (2019) 39–48.
- [24] A.S. Jeevarathinam, J.E. Lemaster, F. Chen, E. Zhao, J.V. Jokerst, Photoacoustic imaging quantifies drug release from nanocarriers via redox chemistry of dye-labeled cargo, *Angew. Chem. Int. Ed.* 59 (12) (2020) 4678–4683.
- [25] J. Zhang, Y. Zhang, Q. Guo, G. Wen, H. Xiao, S. Qi, Y. Wang, H. Zhang, L. Wang, H. Sun, Photoacoustic/fluorescence dual-modality probe for biothiol discrimination and tumor diagnosis in cells and mice, *ACS Sens.* 7 (4) (2022) 1105–1112.
- [26] L.V. Wang, S. Hu, Photoacoustic tomography: in vivo imaging from organelles to organs, *Science* 335 (6075) (2012) 1458–1462.
- [27] J. Zhang, G. Wen, W. Wang, K. Cheng, Q. Guo, S. Tian, C. Liu, H. Hu, Y. Zhang, H. Zhang, Controllable cleavage of C–N bond-based fluorescent and photoacoustic dual-modal probes for the detection of H₂S in living mice, *ACS Appl. Bio Mater.* 4 (3) (2020) 2020–2025.
- [28] Z. Wang, M. Zhan, W. Li, C. Chu, D. Xing, S. Lu, X. Hu, Photoacoustic cavitation-ignited reactive oxygen species to amplify peroxynitrite burst by photosensitization-free polymeric nanocapsules, *Angew. Chem. Int. Ed.* 60 (2021) 4720–4731.
- [29] Z. Wang, M. Zhan, X. Hu, Pulsed laser excited photoacoustic effect for disease diagnosis and therapy, *Chem. Eur. J.* 28 (37) (2022), e202200042.
- [30] H.M. Dao, C.H. Whang, V.K. Shankar, Y.H. Wang, I.A. Khan, L.A. Walker, I. Husain, S.I. Khan, S.N. Murthy, S. Jo, Methylene blue as a far-red light-mediated photocleavable multifunctional ligand, *Chem. Commun.* 56 (2020) 1673–1676.
- [31] J. Bae, L.E. McNamara, M.A. Nael, F. Mahdi, R.J. Doerksen, G.L. Bidwell III, N. I. Hammer, S. Jo, Nitroreductase-triggered activation of a novel caged fluorescent probe obtained from methylene blue, *Chem. Commun.* 51 (2015) 12787–12790.
- [32] Z. Li, Y.F. Wang, C. Zeng, L. Hu, X.J. Liang, Ultrasensitive tyrosinase-activated turn-on near-infrared fluorescent probe with a rationally designed urea bond for selective imaging and photodamage to melanoma cells, *Anal. Chem.* 90 (2018) 3666–3669.
- [33] P. Wei, F. Xue, Y. Shi, R. Strand, H. Chen, T. Yi, A fluoride activated methylene blue releasing platform for imaging and antimicrobial photodynamic therapy of human dental plaque, *Chem. Commun.* 54 (2018) 13115–13118.
- [34] J. Yu, C.H. Hsu, C.C. Huang, P.Y. Chang, Development of therapeutic Au-methylene blue nanoparticles for targeted photodynamic therapy of cervical cancer cells, *ACS Appl. Mater. Interfaces* 7 (2015) 432–441.
- [35] V.P.S. Jesus, L. Raniero, G.M. Lemes, T.T. Bhattacharjee, P.C. Caetano Junior, M. L. Castilho, Nanoparticles of methylene blue enhance photodynamic therapy, *Photodiagnosis Photodyn. Ther.* 23 (2018) 212–217.
- [36] X. Xu, H. Wu, Y. Yang, B. Liu, J. Tian, H. Bao, T. Liu, PLGA-coated methylene blue nanoparticles for photoacoustic imaging and photodynamic/photothermal cascaded precisely synergistic therapy of tumor, *RSC Adv.* 12 (2022) 1543–1549.
- [37] G.N. Makhadmeh, A. Abdul Aziz, K. Abdul Razak, The efficacy of methylene blue encapsulated in silica nanoparticles compared to naked methylene blue for photodynamic applications, *Artif. Cells, Nanomed., Biotechnol.* 44 (2016) 1018–1022.
- [38] A. Fernandez-Lodeiro, J. Djafari, J. Fernandez-Lodeiro, M.P. Duarte, E. Muchagato Mauricio, J.L. Capelo-Martinez, C. Lodeiro, Synthesis of mesoporous silica coated gold nanorods loaded with methylene blue and its potentials in antibacterial applications, *Nanomaterials* 11 (2021) 1338.
- [39] N.S. Kaya, A. Yadav, M. Wehrhold, L. Zuccaro, K. Balasubramanian, Binding kinetics of methylene blue on monolayer graphene investigated by multiparameter surface plasmon resonance, *ACS Omega* 3 (2018) 7133–7140.
- [40] G. Wu, Y.Z. Fang, S. Yang, J.R. Lupton, N.D. Turner, Glutathione metabolism and its implications for health, *J. Nutr.* 134 (2004) 489–492.
- [41] S. Wang, L. Zhang, J. Zhao, M. He, Y. Huang, S. Zhao, A tumor microenvironment-induced absorption red-shifted polymer nanoparticle for simultaneously activated photoacoustic imaging and photothermal therapy, *Sci. Adv.* 7 (2021), eabe3588.
- [42] B. Niu, K. Liao, Y. Zhou, T. Wen, G. Quan, X. Pan, C. Wu, Application of glutathione depletion in cancer therapy: enhanced ROS-based therapy, ferroptosis, and chemotherapy, *Biomaterials* 277 (2021), 121110.
- [43] X. Ling, X. Chen, I.A. Riddell, W. Tao, J. Wang, G. Hollett, S.J. Lippard, O. C. Farokhzad, J. Shi, J. Wu, Glutathione-scavenging poly(disulfide amide) nanoparticles for the effective delivery of Pt(IV) prodrugs and reversal of cisplatin resistance, *Nano Lett.* 18 (7) (2018) 4618–4625.
- [44] Y. Yang, Y. Lu, P.L. Abbaraju, I. Azimi, C. Lei, J. Tang, M. Jambhrunkar, J. Fu, M. Zhang, Y. Liu, C. Liu, C. Yu, Stepwise degradable nanocarriers enabled cascade delivery for synergistic cancer therapy, *Adv. Funct. Mater.* 28 (28) (2018), 1800706.
- [45] X. Meng, J. Deng, F. Liu, T. Guo, M. Liu, P. Dai, A. Fan, Z. Wang, Y. Zhao, Triggered all-active metal organic framework: ferroptosis machinery contributes to the apoptotic photodynamic antitumor therapy, *Nano Lett.* 19 (11) (2019) 7866–7876.
- [46] L.-S. Lin, J. Song, L. Song, K. Ke, Y. Liu, Z. Zhou, Z. Shen, J. Li, Z. Yang, W. Tang, G. Niu, H.-H. Yang, X. Chen, Simultaneous fenton-like ion delivery and glutathione depletion by MnO₂-based nanoagent to enhance chemodynamic therapy, *Angew. Chem. Int. Ed.* 57 (2018) 4902–4906.
- [47] H. Fan, G. Yan, Z. Zhao, X. Hu, W. Zhang, H. Liu, X. Fu, T. Fu, X.B. Zhang, W. Tan, A smart photosensitizer-manganese dioxide nanosystem for enhanced photodynamic therapy by reducing glutathione levels in cancer cells, *Angew. Chem. Int. Ed.* 55 (2016) 5477–5582.
- [48] W. Zhang, J. Lu, X. Gao, P. Li, W. Zhang, Y. Ma, H. Wang, B. Tang, Enhanced photodynamic therapy by reduced levels of intracellular glutathione obtained by employing a nano-MOF with Cu^{II} as the active center, *Angew. Chem. Int. Ed.* 57 (2018) 4891–4896.
- [49] J. An, S. Tang, G. Hong, W. Chen, M. Chen, J. Song, Z. Li, X. Peng, F. Song, W. H. Zheng, An unexpected strategy to alleviate hypoxia limitation of photodynamic therapy by biotinylation of photosensitizers, *Nat. Commun.* 13 (2022) 2225.
- [50] S. Maiti, N. Park, J.H. Han, H.M. Jeon, J.H. Lee, S. Bhuniya, C. Kang, J.S. Kim, Gemcitabine-coumarin-biotin conjugates: a target specific theranostic anticancer prodrug, *J. Am. Chem. Soc.* 135 (2013) 4567–4572.
- [51] Y. Ma, Z. Su, L. Zhou, L. He, Z. Hou, J. Zou, Y. Cai, D. Chang, J. Xie, C. Zhu, W. Fan, X. Chen, S. Ju, Biodegradable metal-organic-framework-gated organosilica for tumor-microenvironment-unlocked glutathione-depletion-enhanced synergistic therapy, *Adv. Mater.* 34 (12) (2022), e2107560.